

## **Lgl resets Par complex membrane loading at mitotic exit to enable asymmetric neural stem cell division**

Bryce LaFoya\*, Sarah E. Welch\*, and Kenneth E. Prehoda<sup>1</sup>

Institute of Molecular Biology  
Department of Chemistry and Biochemistry  
1229 University of Oregon  
Eugene, OR 97403

\*contributed equally

<sup>1</sup>Corresponding author: [prehoda@uoregon.edu](mailto:prehoda@uoregon.edu)

## 1 **Summary**

2 The Par complex regulates cell polarity in diverse animal cells<sup>1-4</sup>, but how its localization is  
3 restricted to a specific membrane domain remains unclear. We investigated how the tumor  
4 suppressor Lethal giant larvae (Lgl) polarizes the Par complex in *Drosophila* neural stem cells  
5 (NSCs or neuroblasts). In contrast to epithelial cells, where Lgl and the Par complex occupy  
6 mutually exclusive membrane domains, Lgl is cytoplasmic when the Par complex is apically  
7 polarized in NSCs<sup>5</sup>. Importantly, we found that Lgl's key function is not in directly regulating  
8 metaphase Par polarity, but rather in removing the Par complex from the membrane at the end  
9 of mitosis, creating a "polarity reset" for the next cell cycle. Without this Lgl-mediated reset, we  
10 found that residual Par complex remains on the basal membrane during subsequent divisions,  
11 disrupting fate determinant polarization and proper asymmetric cell division. These findings  
12 reveal a novel mechanism of polarity regulation by Lgl and highlight the importance of the pre-  
13 polarized state in Par-mediated polarity.

14

## 15 **Introduction**

16 Cortical polarity is a fundamental cellular characteristic that underlies diverse biological  
17 processes, including directional cell migration, tissue organization, and asymmetric cell  
18 division. The Par complex, consisting of Par-6 and atypical Protein Kinase C (aPKC), plays a  
19 pivotal role in establishing and maintaining polarity in a wide range of animal cells, from  
20 epithelial cells to neurons<sup>1-3,6</sup>. The proper localization and function of the Par complex are  
21 particularly critical in stem cells, where asymmetric distribution of cell fate determinants  
22 governs the delicate balance between self-renewal and differentiation. A fundamental question  
23 in cell polarity research is how the Par complex itself is restricted to specific membrane  
24 domains. The tumor suppressor Lethal giant larvae (Lgl) plays a key role in Par polarity by  
25 restricting the Par complex to the proper membrane domain<sup>5,7-10</sup>, but how Lgl controls Par  
26 complex localization remains an open question.

27 Par polarity is the result of a complex interplay of positive and negative regulators. While  
28 factors like Par-3 (Bazooka in *Drosophila*) and Cdc42 ensure that the Par complex is targeted  
29 to the membrane<sup>11-13</sup>, the negative regulation provided by Lgl restricts the complex to a  
30 specific membrane domain. Lgl is thought to perform this critical function by mutual exclusion:  
31 the Par complex and Lgl reciprocally control one another's localization by binding to the  
32 membrane<sup>3,5,7,14</sup>. The mutual exclusion model is exemplified by interphase epithelial cells,

33 where the Par complex is confined to the apical plasma membrane while Lgl occupies the  
34 basolateral domain (Fig. 1A). Loss of either component, Lgl or Par complex, allows the other to  
35 enter the incorrect domain<sup>5,7,9</sup>. How the Par complex excludes Lgl from the Par domain is well-  
36 understood<sup>15-17</sup>, but little is known about how Lgl regulates Par complex localization.

37 Like epithelial cells, proper Par localization in NSCs requires Lgl<sup>4,12,18,19</sup>. In NSCs lacking Lgl  
38 function, the Par complex is localized across the entire membrane instead of being restricted  
39 to its proper domain<sup>12,18</sup>, similar to epithelia. However, a key difference between Lgl's behavior  
40 in NSCs and epithelia lies in Lgl's localization. Instead of localizing to a complementary  
41 membrane domain, Lgl is cytoplasmic when the Par complex is polarized in NSCs<sup>5</sup> (Fig. 1A).  
42 Polarized Par complex with cytoplasmic Lgl has also been observed in sensory organ  
43 precursor (SOP) cells<sup>20</sup>, further challenging the exclusion model. Thus, Lgl's behavior in NSCs  
44 and SOPs indicates that Lgl can regulate Par complex localization without being on the  
45 membrane.

## 46 **Results and Discussion**

### 47 **Patterned Lgl membrane dynamics during NSC mitosis**

48 To gain insight into how Lgl regulates Par complex localization in NSCs, we first examined  
49 Lgl's membrane localization dynamics including how it is restored to the membrane following  
50 mitosis. We imaged Lgl's localization in NSCs from *Drosophila* larval brain explants expressing  
51 Lgl-GFP (expressed by Worniu-GAL4 driven UAS) and Histone H2A-RFP (expressed from its  
52 endogenous locus) using rapid, super-resolution spinning disk confocal microscopy (Fig. 1B).  
53 Lgl removal from the membrane began in early prophase, initiating at a small area near the  
54 apical pole of the cell and spreading rapidly across the membrane such that it appeared to be  
55 completely removed by late prophase (Fig. 1C,D; Video 1). This pattern could be observed  
56 both in medial sections and maximum intensity projections of the full cell volume (Fig. 1E;  
57 Video 1). The full volume data also revealed how Lgl displacement from the membrane was  
58 affected by the membrane structures that are present on the NSC surface<sup>21-23</sup>. Lgl was  
59 enriched in the membrane structures, consistent with their higher membrane density. Lgl  
60 disappeared from the structures as it was displaced from the membrane, while the structures  
61 themselves remained evident when imaging a membrane sensor (Video 1).

62 While Lgl appeared to be completely removed from the membrane when imaging NSCs in  
63 intact tissue, progeny cells adhered to the basal region prevented a definite determination. We

64 imaged individual cultured NSCs that had been dissociated from brains to observe basal Lgl  
65 dynamics in the absence of adhering cells. The Lgl dynamics in dissociated NSCs were  
66 consistent with our initial observations of apically-directed membrane clearing and provided  
67 unambiguous evidence that Lgl is indeed completely removed from the membrane by late  
68 prophase (Fig. 1F,G; Video 1). The patterned Lgl membrane displacement dynamics indicate  
69 that removal is a spatially regulated process, like that observed for SOPs<sup>20</sup>, rather than one in  
70 which it is simultaneously removed from the membrane.

71 NSCs undergo repeated cycles of asymmetric division such that Lgl must be restored to the  
72 membrane at some point to achieve its interphase localization state. We analyzed Lgl  
73 dynamics in both intact brain and dissociated NSCs to determine when and how Lgl is  
74 restored to the membrane following mitosis. Our results showed that Lgl becomes rapidly  
75 restored to the membrane at the completion of mitosis, beginning near the cytokinetic pore  
76 connecting the nascent sibling cells (Fig. 1H-J; Videos 1,3), similar to the dynamics observed in  
77 follicular epithelial cells<sup>24</sup>. Our results provide a detailed description of Lgl's dynamic  
78 localization throughout the cell cycle in NSCs, revealing precise spatial and temporal control of  
79 its membrane association (Fig. 1K).

#### 80 **aPKC removes Lgl from the NSC early in mitosis**

81 Since Lgl is cytoplasmic at metaphase in NSCs, when the Par complex is polarized, we sought  
82 to understand how it transitions between membrane-bound and cytoplasmic states. Evidence  
83 from various cell types indicates that Lgl can be phosphorylated and removed from the  
84 membrane by the Par complex subunit atypical Protein Kinase C (aPKC) but also by the mitotic  
85 kinase Aurora A<sup>5,7</sup>. Aurora A could also regulate Lgl's membrane association indirectly by  
86 influencing aPKC polarity<sup>20,25</sup>. We sought to determine whether one or both kinases are  
87 responsible for the patterned removal of Lgl from the NSC membrane during prophase. To  
88 dissect the relative contributions of aPKC and Aurora A to Lgl removal, we separately inhibited  
89 aPKC or Aurora A activity and assessed the effect on Lgl localization dynamics. We inhibited  
90 aPKC by expressing a UAS-controlled aPKC RNAi specifically in larval brain NSCs using  
91 Worniu-GAL4 driven expression. For Aurora A inhibition, we added the specific inhibitor  
92 MLN8237<sup>7</sup> to the larval brain explant culture media.

93 In NSCs where aPKC was depleted by RNAi, we observed that Lgl removal from the  
94 membrane in mitosis was largely inhibited (Fig. 2A,B; Video 2). Unlike wild-type NSCs, where

95 Lgl was removed from the membrane late in prophase, aPKC RNAi NSCs had persistent Lgl  
96 membrane enrichment throughout mitosis. We did detect a small decrease in apical Lgl  
97 membrane signal beginning in early prophase (Fig. 2A,B) suggesting the presence of residual  
98 aPKC activity or a small contribution from another mechanism. The retention of Lgl on the  
99 membrane in aPKC-depleted cells indicates that aPKC-mediated phosphorylation is the  
100 primary mechanism driving Lgl dissociation from the plasma membrane as NSCs enter mitosis.  
101 Interestingly, Lgl's membrane enrichment during interphase was enhanced in aPKC RNAi  
102 NSCs (Fig. 2A,B), suggesting that Lgl exchanges between the membrane and cytoplasm due  
103 to phosphorylation and dephosphorylation in wild-type NSCs.

104 We also tested if Aurora A activity is required for Lgl membrane displacement as it can directly  
105 phosphorylate Lgl and can also regulate aPKC polarity<sup>5,7,20,25</sup>. Consistent with our results  
106 indicating that aPKC is the dominant kinase responsible for displacement of Lgl from the  
107 membrane in NSCs, we found that inhibition of Aurora A activity with MLN8237 did not cause a  
108 significant difference in Lgl removal from the membrane compared to wild-type NSCs (Fig.  
109 2C,D; Video 2). The patterned removal of Lgl from the membrane proceeded with similar  
110 dynamics and extent as observed in untreated cells. However, we did observe cytokinesis  
111 defects in treated NSCs (Fig. 2C; Video 2) indicating that Aurora A was successfully inhibited.  
112 We conclude that, despite its known ability to phosphorylate Lgl, Aurora A does not participate  
113 in the removal of Lgl from the NSC membrane. This conclusion is consistent with a previous  
114 study demonstrating that Aurora A phosphorylation sites on Lgl aren't required for NSC  
115 membrane displacement<sup>5</sup>.

### 116 **Correlated aPKC and Lgl membrane dynamics**

117 We next sought to determine the degree to which aPKC and Lgl membrane dynamics are  
118 spatially and temporally correlated. The recruitment of aPKC to the membrane in early  
119 prophase is a complex, multistep process where aPKC is initially localized to small domains on  
120 the apical membrane before coalescing into an apical cap by metaphase<sup>26,27</sup>. To determine the  
121 interplay between Lgl's disappearance and aPKC's appearance on the membrane, we  
122 simultaneously imaged aPKC-GFP (expressed from its endogenous promoter) and Lgl-  
123 mCherry (expressed by Worniu-GAL4 driven UAS) in NSCs. This approach allowed us to  
124 directly observe the spatial and temporal dynamics of aPKC recruitment with the pattern of Lgl  
125 removal from the cell membrane. Lgl removal at the apical pole of the NSC was tightly  
126 correlated with the appearance of aPKC at that site (Fig. 3A-C; Video 3). In the apical

127 hemisphere, the appearance of aPKC at the membrane was strongly correlated with Lgl  
128 removal. However, Lgl was also removed from the basal membrane even though aPKC does  
129 not localize there. We conclude that aPKC removes Lgl from the membrane both directly (i.e.  
130 apical membrane) and indirectly (i.e. basal membrane). Indirect removal of basal Lgl by apical  
131 aPKC is likely influenced by factors such as the rate of Lgl diffusion along the plasma  
132 membrane.

133 Near the end of mitosis, aPKC spread along the nascent NSC membrane while being excluded  
134 from the membrane of the smaller nascent neural precursor (NP)<sup>26</sup> (Figure 3D; Video 3). Shortly  
135 after it reached the furrow, aPKC was removed from the membrane. We observed patterned  
136 removal of aPKC from the membrane that was correlated with Lgl's membrane reloading at  
137 mitotic exit (Figs. 1H,I, 3D-F; Video 3). As Lgl accumulated on the basal membrane of the  
138 nascent NSC near the cytokinetic pore, aPKC was removed from the membrane in a  
139 complementary pattern. Lgl continued to spread along the membrane until it occupied both  
140 basal and apical membrane and aPKC was no longer detectable on the membrane (Fig. 3D-F).

#### 141 **Lgl excludes basal aPKC by regulating its interphase membrane association**

142 The mutual exclusion model, which posits that Lgl and the Par complex reciprocally control  
143 each other's localization by occupying opposing membrane domains, does not explain the  
144 behavior of these proteins in SOPs<sup>20</sup> or NSCs<sup>5</sup> (Fig. 3A). The primary inconsistency is the  
145 metaphase polarized state when the Par complex is polarized while Lgl is cytoplasmic.  
146 However, it is also not known whether Lgl is responsible for excluding aPKC from the  
147 membrane during interphase in NSCs. To gain insight into how Lgl regulates Par complex  
148 localization in these contexts, we examined aPKC localization in NSCs expressing Lgl RNAi  
149 (Worniu-GAL4 driven UAS). While aPKC is excluded from the cell membrane during interphase  
150 in wild-type NSCs, aPKC was not removed from the membrane at the end of mitosis in Lgl  
151 RNAi NSCs, remaining on the membrane throughout interphase and the subsequent mitosis  
152 (Fig. 4A-D; Video 4). However, the accumulation of aPKC at the apical membrane during early  
153 mitosis did not require Lgl, occurring both in wild-type and Lgl RNAi NSCs (Fig. 4A,C; Video 4).  
154 Apical enrichment caused aPKC to be polarized in both contexts at metaphase (Fig. 4E), with  
155 the key difference that Lgl RNAi NSCs had detectable basal aPKC at this stage (Fig. 4D). We  
156 conclude that Lgl is required to remove aPKC from the membrane at mitotic exit in NSCs but is  
157 not required for apical enrichment of the Par complex during early mitosis.

## 158 **Lgl resets Par polarity for subsequent asymmetric NSC division**

159 Our results provide a more nuanced view of Lgl function in Par polarity than provided by the  
160 mutual exclusion model. Rather than directly regulating metaphase Par polarity by occupying  
161 an opposing membrane domain, Lgl acts much earlier in the cell cycle to clear the Par complex  
162 from the NSC membrane at the end of mitosis. This mechanism ensures that each cell cycle  
163 begins without Par complex on the membrane (Fig. 4F). The importance of this “polarity reset”  
164 can be seen in NSCs where the Par complex isn’t removed from the membrane. In NSCs  
165 lacking Lgl function, the Par complex remains on the membrane after mitosis. Shortly after  
166 mitotic entry, the Par complex becomes enriched at the apical membrane, like in wild-type  
167 NSCs (Fig. 4C,E). However, residual basal Par complex from interphase (Fig. 4D) prevents fate  
168 determinant polarization<sup>18</sup>, disrupting asymmetric cell division. Thus, Lgl is not required for Par  
169 polarity in NSCs but instead ensures the Par complex is removed from the membrane when  
170 polarization begins in early mitosis. In other words, Par polarity is insufficient to support NSC  
171 asymmetric division – the Par complex must be on the apical membrane and not on the basal  
172 membrane. Basal Par complex, even at the reduced levels we observed compared to apically-  
173 enriched complex, disrupts fate determinant polarity and asymmetric cell division<sup>18</sup>.

174 While the metaphase polarized state has long been the focus of NSC asymmetric cell division  
175 research<sup>2,28-31</sup>, our results highlight the importance of the progression from mitosis to  
176 interphase to the process. Asymmetric cell division couples transitions in cell fate to the  
177 division cycle and fate transitions likely occur at or near mitotic exit. Consistent with the  
178 importance of this cell cycle phase, fate determinants are activated shortly after the end of  
179 mitosis<sup>32</sup>. The midbody that forms in the intercellular bridge connecting nascent siblings plays  
180 a key role in mediating asymmetric fate specification<sup>32</sup>. Intriguingly, Lgl membrane reloading  
181 and the concomitant displacement of aPKC into the cytoplasm begins at or near the  
182 midbody (Fig. 3D-F) suggesting that fate specification and resetting polarity could be regulated  
183 by the same pathways.

184 The mechanism by which Lgl removes aPKC from the membrane at the end of mitosis remains  
185 an intriguing question. There are several possibilities based on our current understanding of Lgl  
186 and aPKC. One potential mechanism is that Lgl, upon its rapid return to the membrane post-  
187 mitosis, could act as a competitive inhibitor for aPKC membrane binding sites. Lgl's strong  
188 affinity for the membrane<sup>15,16</sup> might allow it to outcompete aPKC and displace it from the  
189 membrane. Alternatively, Lgl could recruit or activate a phosphatase that dephosphorylates

190 aPKC or its binding partners, thereby reducing aPKC's affinity for the membrane. Further  
191 investigation into these potential mechanisms will be crucial for fully understanding Lgl's role in  
192 polarity regulation.

### 193 **Figure Legends**

194 Figure 1 Patterned Lgl displacement and reloading during neural stem cell asymmetric division  
195 (A) Mutual exclusion model for Par polarity. In this model, the Par complex (comprised of Par-6  
196 and atypical Protein Kinase C or aPKC) establishes a mutually exclusive membrane domain  
197 with Lethal giant larvae (Lgl), wherein the presence of one protein on the membrane prevents  
198 the binding of the other. This model is consistent with the localization pattern in epithelial cells  
199 but not *Drosophila* neural stem cells (NSCs) and sensory organ precursors, where the Par  
200 complex becomes polarized during mitosis while Lgl remains cytoplasmic.

201 (B) Imaging *Drosophila* larval brain neural stem cells (NSCs). The larval central nervous system  
202 (CNS), including the brain lobes and ventral nerve cord, was extracted from third-instar larvae  
203 (L3). Neural stem cells (NSCs), characterized by their relatively large size, specific locations  
204 within the brain, and expression of tissue-specific transgenes, were either imaged within the  
205 intact CNS or, alternatively, the tissue was dissociated to isolate and image the NSCs  
206 individually.

207 (C) Removal of Lgl from the plasma membrane in early mitosis in an NSC from the intact CNS.  
208 Frames from Video 1 are shown. The NSC (marked with asterisk) is expressing Lgl-GFP  
209 (expressed from *Worniu-GAL4* driven UAS) and Histone H2A (*His2a-RFP*). Time is shown  
210 relative to anaphase onset.

211 (D) Patterned removal of Lgl from the plasma membrane in early mitosis. The ratio of  
212 membrane-to-cytoplasmic Lgl is presented for ten distinct neural stem cells (NSCs) in the  
213 apical and lateral regions during early mitosis, when Lgl was first cleared from the apical  
214 membrane. The Gardner-Altman estimation plot illustrates the paired measurements for each  
215 NSC. Additionally, the 95% confidence interval is displayed in the mean difference  
216 comparison, along with the corresponding bootstrap distribution from which it was derived.

217 (E) A 3D projection of Lgl dynamics during early mitosis. Frames from Video 1 are shown. The  
218 NSC is expressing Lgl-GFP (expressed from *Worniu-GAL4* driven UAS). The top row depicts a  
219 medial optical section. The bottom row depicts a maximum intensity projection (MIP) of optical  
220 sections across one hemisphere of the cell. Time is shown relative to anaphase onset.



221 (F) Removal of Lgl from the plasma membrane in early mitosis in an NSC dissociated from the  
222 CNS. Frames from Video 1 are shown. The NSC is expressing Lgl-GFP (expressed from  
223 Worniu-GAL4 driven UAS) and Histone H2A (His2a-RFP). Time is shown relative to anaphase  
224 onset.

225 (G) The timing of the clearance of the basal Lgl membrane signal, represented by a membrane-  
226 to-cytoplasmic signal ratio close to one, is presented for three dissociated neural stem cells  
227 (NSCs) in relation to metaphase.

228 (H) Lgl reloading to the plasma membrane in early interphase in an NSC from an intact CNS.  
229 Frames from Video 1 are shown as in (C). Time is shown relative to anaphase onset.

230 (I) Lgl reloading to the plasma membrane in early interphase in an NSC dissociated from the  
231 CNS. Frames from Video 1 are shown as in (F).

232 (J) Lgl patterned membrane reloading in early interphase. The ratio of membrane-to-  
233 cytoplasmic Lgl is shown for two time points: one at the conclusion of anaphase and another  
234 during interphase. Measurements were taken near the cytokinetic midbody as well as along the  
235 lateral and apical membranes.

236 (K) Schematic representation of Lgl membrane dynamics in neural stem cells (NSCs). During  
237 interphase, Lgl is distributed across the NSC membrane. In early mitosis, membrane clearing  
238 begins starting at the apical pole and fully clearing by prophase. Membrane reloading of Lgl  
239 begins in early interphase beginning near the midbody region.

240 Figure 2 aPKC but not Aurora A is required for Lgl removal from the NSC membrane in early  
241 mitosis

242 (A) Lgl dynamics in an NSC from the intact central nervous system expressing aPKC RNAi.  
243 Frames from Video 2 are shown. The NSC is expressing Lgl-GFP and aPKC RNAi (both  
244 expressed from Worniu-GAL4 driven UAS). Time is shown relative to anaphase onset. The  
245 same timepoints are shown from an NSC expressing Lgl-GFP, but not expressing aPKC RNAi  
246 for a wild-type ("WT") comparison.

247 (B) aPKC is required for Lgl removal from the membrane in early mitosis. The Gardner-Altman  
248 estimation plot displays error bars indicating one standard deviation (with the gap representing  
249 the mean). The bar in the mean difference comparison reflects the bootstrap 95% confidence  
250 interval. Each data point corresponds to a measurement taken from a distinct NSC.

251 (C) Lgl dynamics in an NSC from the intact central nervous system incubated with the specific  
252 Aurora A inhibitor MLN8237. Frames from Video 2 are shown. The NSC is expressing Lgl-GFP  
253 along with aPKC RNAi, both driven by Worniu-GAL4 and UAS. Arrowheads indicate furrow

254 retraction during late cytokinesis, providing evidence of drug effectiveness. The time is shown  
255 relative to anaphase onset. For comparison, similar timepoints are depicted for an NSC  
256 incubated with DMSO alone (vehicle control).

257 (D) Aurora A inhibition does not detectably influence Lgl membrane displacement in early  
258 mitosis. Lgl apical membrane-to-cytoplasmic ration is shown for reated with either MLN8237 or  
259 the vehicle control (DMSO) during interphase, prophase, and metaphase. The Gardner-Altman  
260 estimation plot displays error bars representing one standard deviation (with the gap indicating  
261 the mean). The bar representing the mean difference comparison reflects the bootstrap 95%  
262 confidence interval.

263 Figure 3 Correlated aPKC and Lgl NSC membrane dynamics

264 (A) Lgl and aPKC dynamics in an NSC from the intact central nervous system (CNS) during Lgl  
265 membrane clearance at mitotic entry. Frames from Video 3 are shown. The NSC is expressing  
266 aPKC-GFP (expressed from its native promoter) and Lgl-mCherry (expressed from Worniu-  
267 GAL4 driven UAS). Time is indicated relative to anaphase onset.

268 (B) Lgl patterned removal at mitotic entry. The membrane-to-cytoplasmic ratio of Lgl was  
269 assessed both before and during the clearance of Lgl from the membrane, specifically at the  
270 apical and lateral membrane. The Gardner-Altman estimation plot displays error bars that  
271 indicate one standard deviation, with the gap denoting the mean value. The bar in the mean  
272 difference comparison illustrates the bootstrap 95% confidence interval. Each point on the plot  
273 corresponds to a measurement taken from a distinct NSC. Time is indicated relative to  
274 anaphase onset.

275 (C) aPKC is apically enriched when Lgl begins clearing from the membrane at mitotic entry. The  
276 membrane-to-cytoplasmic ratio of aPKC is presented both before and during the clearance of  
277 Lgl from the membrane, measured at the apical and lateral membrane. Plotted as in (B)

278 (D) The dynamics of Lgl and aPKC in an NSC from the intact CNS during the clearance of  
279 aPKC from the membrane at mitotic exit are illustrated with frames extracted from Video 3. The  
280 NSC is expressing aPKC-GFP driven by its native promoter and Lgl-mCherry expressed by  
281 Worniu-GAL4 driven UAS. Time is indicated relative to the beginning of the imaging session.

282 (E) Lgl patterned membrane reloading at mitotic exit. At mitotic exit, as aPKC begins to clear  
283 from the membrane, Lgl is basally enriched at the site where the cytokinetic furrow reorganizes  
284 into the midbody. The ratio of membrane-to-cytoplasmic Lgl is presented both before and  
285 during the clearing of aPKC from the membrane, measured at the lateral membrane and near  
286 the furrow (as the midbody forms). The data is plotted as shown in panel (B).

287 (F) aPKC patterned removal at mitotic exit. The ratio of membrane-to-cytoplasmic aPKC is  
288 presented both before and during the clearing of aPKC from the membrane, measured at the  
289 lateral membrane and near the furrow (as the midbody forms). The data is plotted as shown in  
290 panel (B)

291 Figure 4 Lgl resets NSC polarity by removing aPKC from the membrane at mitotic exit

292 (A) aPKC dynamics in an NSC from the intact central nervous system expressing Lgl RNAi. The  
293 frames from Video 4 are presented, showcasing an NSC expressing aPKC-GFP, driven by its  
294 native promoter, and Lgl RNAi, induced by Worniu-GAL4 driving UAS. Arrowheads indicate the  
295 presence of basal aPKC before and during mitosis. Time is indicated relative to the onset of  
296 anaphase. For comparison, an NSC that does not express Lgl RNAi (wild-type "WT") is shown  
297 at corresponding time points.

298 (B) Lgl is required to remove aPKC from the membrane during the return to interphase. A  
299 comparison of apical aPKC membrane enrichment in NSCs both expressing and not  
300 expressing Lgl RNAi during interphase, prophase, and metaphase stages. A Gardner-Altman  
301 estimation plot illustrates the data across three distinct NSC divisions. Error bars indicate one  
302 standard deviation, with the gap representing the mean. The bar in the mean difference  
303 comparison reflects the bootstrap 95% confidence interval.

304 (C) aPKC is apically enriched at metaphase in Lgl RNAi NSCs. Comparing apical aPKC  
305 membrane enrichment at prophase and metaphase in Lgl RNAi expressing NSCs. Gardner-  
306 Altman estimation plot as in (B).

307 (D) Lgl is required to remove aPKC from the basal membrane at metaphase. Comparison of  
308 basal aPKC membrane enrichment during metaphase in NSCs expressing Lgl RNAi versus  
309 those not expressing it. Gardner-Altman estimation plot as in (B).

310 (E) Lgl is not required for metaphase aPKC polarity. The ratio of apical-to-cytoplasmic aPKC to  
311 basal-to-cytoplasmic aPKC during metaphase is depicted for three distinct NSC divisions.  
312 Error bars indicate one standard deviation, with the gap representing the mean value.

313 (F) Polarity reset model for Lgl function in NSC asymmetric division. Lgl plays a crucial role in  
314 early interphase by removing the Par complex from the membrane, thereby establishing a  
315 cleared state essential for resetting polarity. The importance of clearing the Par complex from  
316 the membrane during each cell cycle is particularly evident in mitosis. Starting mitosis in a  
317 cleared state ensures that the Par complex binds exclusively to the apical membrane through  
318 its apical targeting mechanisms. As a result, the fate determinants can effectively polarize to  
319 the basal membrane without interference from the Par complex. Without Lgl, the Par complex

320 persists on the membrane throughout interphase. During early mitosis, the Par complex  
321 accumulates at the apical membrane, similar to what occurs in wild-type NSCs, resulting in a  
322 polarized distribution. However, in this scenario, residual Par complex remains on the basal  
323 membrane during mitosis, effectively preventing fate determinants from binding to the basal  
324 membrane as they normally would.

## 325 **Resource Availability**

### 326 **Lead Contact**

327 Contact the Lead Contact, Kenneth Prehoda ([prehoda@uoregon.edu](mailto:prehoda@uoregon.edu)), for further information or  
328 to request resources and reagents.

### 329 **Materials Availability**

330 No new reagents were generated in this study.

### 331 **Data and Code Availability**

332 Raw data available from the corresponding author on request.

## 333 **Experimental Model and Subject Details**

334

### 335 **Fly Strains**

336

337 Tissue-specific expression of UAS controlled transgenes in NSCs was achieved using a  
338 Worniu-GAL4 driver line<sup>33</sup>. Lgl dynamics were imaged using UAS-Lgl-GFP or UAS-Lgl-mCherry  
339 (as noted in figure and video legends). Plasma membrane dynamics were imaged using the  
340 membrane marker UAS-PLC $\delta$ -PH-mCherry, which expresses the pleckstrin homology domain  
341 of human PLC $\delta$  tagged with mCherry and binds to the plasma membrane lipid phosphoinositide  
342 PI(4,5)P<sub>2</sub>. Chromosome dynamics were monitored using the marker His2A-RFP. Imaging of  
343 aPKC was achieved using a BAC-encoded aPKC-GFP<sup>34</sup>. Worniu-GAL4 was used to express  
344 UAS-RNAi against aPKC and Lgl in NSCs. Knockdown was enhanced through the co-  
345 expression of UAS-Dicer2.

346

### 347 **Method Details**

348

#### 349 **Live Imaging**

350 Third instar larvae were incubated at 29°C for at least 48 hours prior to imaging and dissection.  
351 Larvae were dissected in Schneider's Insect Media (SIM) to obtain intact central nervous  
352 system explants, which were then mounted on a sterile poly-D-lysine coated 35mm glass  
353 bottom dish (ibidi Cat#81156) containing modified minimal hemolymph-like solution (HL3.1).  
354 Larval brain explants were imaged using a Nikon Eclipse Ti-2 Yokogawa CSU-W1 SoRa  
355 spinning disk microscope with dual Photometrics Prime BSI sCMOS cameras, utilizing a 60x  
356 water immersion objective. GFP-tagged proteins were visualized using 488 nm illumination,  
357 while RFP and mCherry tags were visualized using 561 nm illumination. Super-resolution

358 images were captured via SoRa (super-resolution through optical photon reassignment)  
359 optics<sup>35</sup>. NSCs were identified based on size, location within the central nervous system, and  
360 expression of Worniu-GAL4 driven transgenes.

361  
362 To acquire “dissociated NSCs”, *Drosophila* central nervous systems were collected from third  
363 instar larvae and incubated for 30 min at 30°C in Schneider’s Insect Medium containing 1  
364 mg/mL Papain and 1 mg/mL Collagenase. After incubation, mechanical dissociation was  
365 performed by flushing medium/brains through a pipette tip. The resulting cell suspension was  
366 then pelleted using gentle centrifugation and washed 3 times with culture medium consisting of  
367 Schneider’s Insect Medium containing 10% synthetic fetal bovine serum, 20 mM Glutamine,  
368 0.05 mg/mL Glutathione, and 0.01 mg/mL Insulin. After the final wash step, cells were  
369 resuspended and plated in culture medium consisting of Schneider’s Insect Medium containing  
370 10% synthetic fetal bovine serum, 20 mM Glutamine, 0.05 mg/mL Glutathione, and 0.01 mg/mL  
371 Insulin and imaged with a Nikon Eclipse Ti-2 Yokogawa CSU-W1 SoRa spinning disk  
372 microscope with dual Photometrics Prime BSI sCMOS cameras, using a 60x water immersion  
373 objective.

### 374 375 **Pharmacological Inhibition**

376  
377 The selective Aurora A inhibitor MLN8237 (Alisertib) was solubilized in DMSO and used at a  
378 working concentration of 15  $\mu$ m in all relevant experiments.

### 379 380 **Image Processing and Analysis**

381 Imaging data was processed using ImageJ (FIJI package). To correct for photobleaching, the  
382 bleach correction tool was used.

383  
384 Quantification for Fig. 1D: To quantify the dynamics underlying Lgl’s removal from the plasma  
385 membrane during early mitosis in NSCs within intact central nervous systems, we used ImageJ  
386 to acquire membrane:cytoplasmic ratios for Lgl-GFP signal intensity. To do this, we first  
387 measured Lgl membrane intensity by drawing a line with a 5 pixel width perpendicular to the  
388 membrane traversing from outside the NSC into the cytoplasm at two different locations, the  
389 apical pole and lateral membrane. Lgl membrane signal was quantified using the peak signal  
390 intensity along the line. Lgl cytoplasmic signal intensity was measured by taking the average  
391 signal intensity within a square ROI (region of interest) drawn inside the NSC cytoplasm, being  
392 careful to avoid sampling the nuclear compartment. These measurements allowed us to  
393 compare the apical membrane:cytoplasmic ratios to the lateral membrane:cytoplasmic ratios as  
394 NSCs moved through early mitosis. The figure depicts the lateral membrane:cytoplasmic ratio at  
395 the frame when the apical membrane:cytoplasmic ratio reached  $\sim$ 1 (i.e. Lgl no longer detectable  
396 at the apical pole) for each NSC (n = 10).

397  
398 Quantification for Figure 1G:

399 To quantify the dynamics underlying Lgl’s removal from the basal plasma membrane, we  
400 measured the basal membrane:cytoplasmic ratio for Lgl-GFP signal intensity in dissociated  
401 NSCs. Dissociated NSCs provided a clearer view of the basal membrane compared to NSCs  
402 within intact central nervous systems, where the basal NSC membrane is obscured by the  
403 cluster of progeny cells in this region. The figure depicts the time relative to anaphase onset  
404 when the basal membrane:cytoplasmic ratio reached  $\sim$ 1 (i.e. Lgl no longer detectable at the  
405 basal pole) for each NSC (n = 3). Anaphase onset was determined by using the chromosome  
406 marker His2a-RFP to identify the frame when chromosomes aligned at the metaphase plate

407 began to separate.

408

409 Quantification for Figure 1J:

410 To quantify the dynamics underlying Lgl's rebinding to the plasma membrane during mitotic exit  
411 and interphase return, we measured membrane:cytoplasmic ratios for Lgl-GFP signal intensity  
412 in dissociated NSCs. Dissociated NSCs provided a clearer view of the basal membrane  
413 compared to NSCs within intact central nervous systems, where the basal NSC membrane is  
414 obscured by the cluster of progeny cells in this region. During mitotic exit and interphase return,  
415 cytokinesis is still underway and the nascent sibling cells remain connected by an intercellular  
416 bridge containing the cytokinetic pore<sup>32</sup>. Membrane:cytoplasmic ratios were measured at three  
417 different locations along the nascent NSC membrane, near the cytokinetic pore (the most basal  
418 point of the nascent NSC membrane), the lateral membrane of the nascent NSC, and at the  
419 apical pole of the nascent NSC. These measurements were performed at the end of anaphase  
420 (when the 2 sets of chromosomes had finished moving apart), early interphase, and later in  
421 interphase.

422 Quantification for Figure 2B: To quantify the effects of aPKC knockdown on Lgl's membrane  
423 binding over the course of the cell cycle, apical membrane:cytoplasmic ratios for Lgl-GFP signal  
424 intensity were measured (as described in Fig. 1D). Ratios were measured at three different time  
425 points in the cell cycle. In all the NSCs we sampled, at 15 minutes before nuclear envelope  
426 breakdown (NEB) no NSC had begun the rounding up process that marks mitotic entry. We  
427 therefore used 15 minutes prior to NEB as the "interphase" time point. NSCs were in the  
428 process of rounding up at 7 minutes prior to NEB, and we therefore used this as the "prophase"  
429 time point. We used the frame before anaphase onset as the "metaphase" time point. NSCs  
430 expressing aPKC RNAi were compared to control cells not expressing RNAi (wild-type).

431 Quantification for Figure 2D: To quantify the effects of Aurora A inhibition on Lgl's removal from  
432 the plasma membrane during early mitosis apical membrane:cytoplasmic ratios for Lgl-GFP  
433 signal intensity were measured (as described in Fig. 1D). "Prophase" measurements were  
434 taken at 6 minutes and 40 seconds prior to NEB. "Metaphase" measurement were taken at 20  
435 seconds prior to anaphase onset. NSCs treated with the Aurora A inhibitor solubilized in DMSO  
436 were compared to control cells treated with DMSO alone.

437 Quantifications for Figure 3B and 3C: To determine if Lgl's removal from the apical membrane is  
438 spatially and temporally correlated with the recruitment of aPKC to the apical membrane during  
439 mitotic entry, we used NSCs expressing Lgl-mCherry and aPKC-GFP (n = 3) to measure the  
440 lateral and apical membrane:cytoplasmic ratio for both aPKC and Lgl at the frame in which  
441 apical Lgl-mCherry signal reached the limit of detection (Lgl membrane:cytoplasmic ratio ~ 1).  
442 Figure 3B depicts the lateral and apical membrane:cytoplasmic ratio of Lgl-mCherry signal  
443 intensity. Figure 3C depicts the lateral and apical membrane:cytoplasmic ratio of aPKC-GFP  
444 signal intensity.

445 Quantifications for Figure 3E and 3F: To determine if the removal of aPKC from the membrane  
446 is spatially and temporally correlated with the recruitment of Lgl to the membrane, we performed  
447 dual imaging of NSCs expressing Lgl-mCherry and aPKC-GFP (n = 5). The quantifications  
448 depict measurements taken during mitotic exit, at the frame in which aPKC-GFP signal near the  
449 cytokinetic pore of the nascent NSC reached the limit of detection (membrane:cytoplasmic ratio  
450 ~1). Figure 3E compares the membrane:cytoplasmic ratio of Lgl-mCherry signal intensity at two

451 different locations on the nascent NSC, at the basal membrane of the nascent NSC (near the  
452 cytokinetic pore) and the lateral membrane. Figure 3F compares the membrane:cytoplasmic  
453 ratio of aPKC-GFP signal intensity at two different locations on the nascent NSC, at the basal  
454 membrane of the nascent NSC (near the cytokinetic pore) and the lateral membrane.

455 Quantification for Figure 4B: To quantify the effects of Lgl knockdown on aPKC localization at  
456 the apical membrane, apical membrane:cytoplasmic ratios for aPKC-GFP signal intensity were  
457 measured at interphase (15 minutes prior to NEB), prophase (7 minutes prior to NEB), and  
458 metaphase (1 minute before anaphase onset). NSCs expressing Lgl-RNAi (n = 3) were  
459 compared to wild-type NSCs (n = 3).

460 Quantification for Figure 4C: To quantify the effects of Lgl knockdown on aPKC localization at  
461 the basal membrane, basal membrane:cytoplasmic ratios for aPKC-GFP signal intensity were  
462 measured at metaphase (1 minute before anaphase onset). NSCs expressing Lgl-RNAi (n = 3)  
463 were compared to wild-type NSCs (n = 3).

464 Quantification for Figure 4D: To quantify the effects of Lgl knockdown on the localization of  
465 aPKC to the basal membrane, the basal membrane:cytoplasmic ratio for aPKC-GFP signal  
466 intensity was measured at metaphase (1 minute before anaphase onset). NSCs expressing Lgl-  
467 RNAi (n = 3) and compared to wild-type NSCs (n = 3).

468 Quantification for Figure 4E: To quantify the effects of Lgl knockdown on aPKC polarity, aPKC  
469 signal intensity at the apical and basal poles were compared. The apical membrane:cytoplasmic  
470 and basal membrane:cytoplasmic ratio for aPKC-GFP signal intensity was measured at  
471 metaphase (1 minute before anaphase onset). To calculate the apical:basal ratio, the apical  
472 membrane:cytoplasmic ratio was divided by the basal membrane:cytoplasmic ratio. NSCs  
473 expressing Lgl-RNAi (n = 3) were compared to wild-type NSCs (n = 3).

474  
475

## Statistical Analysis

476 Gardner-Altman estimation plots and 95% confidence intervals of datasets were prepared using  
477 the DABEST package<sup>36</sup>. Statistical details can be found in the relevant figure legends.

## Key Resources Table

REAGENT or RESOURCE	SOURCE	IDENTIFIER
<b>Experimental Model: Fly Strains</b>		
aPKC-GFP	François Schweisguth Lab <sup>34</sup>	
UAS-Lgl-GFP	Jürgen A. Knoblich Lab <sup>20</sup>	
Histone H2a-RFP (His2a-RFP) (chromosome marker)	Bloomington <i>Drosophila</i> Stock Center (BDSC)	BDSC Cat# 23650 RRID: BDSC 23650
Worniu-GAL4 (NSC driver line)	Chris Q. Doe Lab	
aPKC-RNAi	Bloomington <i>Drosophila</i> Stock Center (BDSC)	BDSC Cat#67204 RRID: BDSC 67204
Lgl-RNAi	Bloomington <i>Drosophila</i> Stock Center (BDSC)	BDSC Cat#38989 RRID: BDSC 38989
UAS-Lgl-mCherry	Jürgen A. Knoblich Lab	

UAS-PLC $\delta$ -PH-mCherry (membrane marker)	Bloomington <i>Drosophila</i> Stock Center (BDSC)	BDSC Cat#51658 RRID: BDSC 51658
<b>Pharmacological Inhibitors</b>		
MLN8237 (Alisertib)	Selleckchem	Cat#S1133

479

## 480 **Video Legends**

### 481 **Video 1: Patterned Lgl membrane displacement and reloading during neural stem cell** 482 **(NSC) divisions**

483 *Part 1: Lgl dynamics in NSCs (imaged in intact central nervous systems).* Super-resolution  
484 videos of NSCs expressing Lgl-GFP (Lgl) and His2a-RFP (His2a). Time relative to anaphase  
485 onset is indicated. 3 medial section videos of dividing NSCs within intact central nervous  
486 systems are shown.

487 *Part 2: Lgl dynamics in dissociated NSCs.* Super-resolution videos of dissociated NSCs  
488 expressing Lgl-GFP (Lgl) and His2a-RFP (His2a). Time relative to anaphase onset is indicated.  
489 3 medial section videos of dividing dissociated NSCs are shown.

490 *Part 3: 3D projections and medial sections of Lgl and membrane dynamics in NSCs.* Super-  
491 resolution videos of NSCs expressing Lgl-GFP (Lgl) and the membrane marker PLC $\delta$ -PH-  
492 mCherry (membrane). Time relative to nuclear envelope breakdown (NEB) is indicated. 3D  
493 projections and medial sections are shown for 3 dividing NSCs within intact central nervous  
494 systems.

### 495 **Video 2: The effects of aPKC knockdown and Aurora A inhibition on Lgl dynamics**

496 *Part 1: The effects of aPKC knockdown on Lgl dynamics.* Super-resolution videos of NSCs  
497 expressing Lgl-GFP (Lgl) and aPKC RNAi. Time relative to anaphase onset is indicated. Medial  
498 sections are shown for 6 dividing NSCs within intact central nervous systems.

499 *Part 2: Lgl dynamics in NSCs (wild-type control).* Super-resolution videos of NSCs expressing  
500 Lgl-GFP (Lgl). Time relative to anaphase onset is indicated. Medial sections are shown for 6  
501 dividing NSCs within intact central nervous systems.

502 *Part 3: Lgl dynamics in NSCs treated with Aurora A inhibitor.* Super-resolution videos of NSCs  
503 expressing Lgl-GFP (Lgl) and His2a-RFP (His2a) and treated with Aurora A inhibitor. Time  
504 relative to anaphase onset is indicated. Medial sections are shown for 3 dividing NSCs within  
505 intact central nervous systems.

506 *Part 4: Lgl dynamics in NSCs treated with DMSO.* Super-resolution videos of NSCs expressing  
507 Lgl-GFP (Lgl) and His2a-RFP (His2a) and treated with DMSO (vehicle control). Time relative to  
508 anaphase onset is indicated. Medial sections are shown for 3 dividing NSCs within intact central  
509 nervous systems.

### 510 **Video 3: Dual imaging of Lgl and aPKC dynamics in dividing NSCs**



511 *Part 1: Lgl and aPKC dynamics during mitotic entry.* Super-resolution videos of NSCs  
512 expressing aPKC-GFP (aPKC) and Lgl-mCherry (Lgl). Time relative to anaphase onset is  
513 indicated. Medial sections are shown for 3 dividing NSCs within intact central nervous systems.

514 *Part 2: Lgl and aPKC dynamics during mitotic exit.* Super-resolution videos of NSCs expressing  
515 aPKC-GFP (aPKC) and Lgl-mCherry (Lgl). Time relative to the start of imaging is indicated.  
516 Medial sections are shown for 4 dividing NSCs within intact central nervous systems.

#### 517 **Video 4: The effects of Lgl knockdown on aPKC dynamics**

518 *Part 1: aPKC dynamics in NSCs expressing Lgl RNAi.* Super-resolution videos of NSCs  
519 expressing aPKC-GFP (aPKC) and Lgl-RNAi. Time relative to anaphase onset is indicated.  
520 Medial sections are shown for 3 dividing NSCs within intact central nervous systems.

521 *Part 2: aPKC dynamics in NSCs (wild-type control).* Super-resolution videos of NSCs  
522 expressing aPKC-GFP (aPKC). Time relative to anaphase onset is indicated. Medial sections  
523 are shown for 3 dividing NSCs within intact central nervous systems.

#### 524 **Acknowledgments**

525 We thank Eurico Morais-de-Sá for helpful discussions, Sarah Siegrist for a detailed dissociated  
526 NSC protocol, and Adam Fries for maintaining the microscope used in this study. This work was  
527 supported by NIH grants R35GM127092 and K99GM147601.

#### 528 **Author Contributions**

529 B.L., S.E.W., and K.E.P. designed the experiments. B.L. and S.E.W. performed the  
530 experiments. B.L., S.E.W., and K.E.P analyzed the data, prepared the figures, and wrote the  
531 manuscript.

#### 532 **Declaration of Interests**

533 The authors declare no competing interests.

#### 534 **References**

- 535 1. Lang, C.F., and Munro, E. (2017). The PAR proteins: from molecular circuits to dynamic self-  
536 stabilizing cell polarity. *Dev. Camb. Engl.* *144*, 3405–3416. <https://doi.org/10.1242/dev.139063>.
- 537 2. Sunchu, B., and Cabernard, C. (2020). Principles and mechanisms of asymmetric cell division. *Dev.*  
538 *Camb. Engl.* *147*, dev167650. <https://doi.org/10.1242/dev.167650>.
- 539 3. Buckley, C.E., and St Johnston, D. (2022). Apical-basal polarity and the control of epithelial form and  
540 function. *Nat. Rev. Mol. Cell Biol.* *23*, 559–577. <https://doi.org/10.1038/s41580-022-00465-y>.
- 541 4. Prehoda, K.E. (2009). Polarization of *Drosophila* neuroblasts during asymmetric division. *Cold Spring*  
542 *Harb. Perspect. Biol.* *1*, a001388. <https://doi.org/10.1101/cshperspect.a001388>.
- 543 5. Bell, G.P., Fletcher, G.C., Brain, R., and Thompson, B.J. (2015). Aurora kinases phosphorylate Lgl to  
544 induce mitotic spindle orientation in *Drosophila* epithelia. *Curr. Biol. CB* *25*, 61–68.  
545 <https://doi.org/10.1016/j.cub.2014.10.052>.

- 546 6. Venkei, Z.G., and Yamashita, Y.M. (2018). Emerging mechanisms of asymmetric stem cell division. *J.*  
547 *Cell Biol.* <https://doi.org/10.1083/jcb.201807037>.
- 548 7. Carvalho, C.A., Moreira, S., Ventura, G., Sunkel, C.E., and Morais-de-Sá, E. (2015). Aurora A triggers  
549 Lgl cortical release during symmetric division to control planar spindle orientation. *Curr. Biol.* *CB* 25,  
550 53–60. <https://doi.org/10.1016/j.cub.2014.10.053>.
- 551 8. Grifoni, D., Garoia, F., Bellosta, P., Parisi, F., De Biase, D., Collina, G., Strand, D., Cavicchi, S., and  
552 Pession, A. (2007). aPKCzeta cortical loading is associated with Lgl cytoplasmic release and tumor  
553 growth in *Drosophila* and human epithelia. *Oncogene* 26, 5960–5965.  
554 <https://doi.org/10.1038/sj.onc.1210389>.
- 555 9. Yamanaka, T., Horikoshi, Y., Izumi, N., Suzuki, A., Mizuno, K., and Ohno, S. (2006). Lgl mediates  
556 apical domain disassembly by suppressing the PAR-3-aPKC-PAR-6 complex to orient apical  
557 membrane polarity. *J. Cell Sci.* 119, 2107–2118. <https://doi.org/10.1242/jcs.02938>.
- 558 10. Moreira, S., and Morais-de-Sá, E. (2016). Spatiotemporal phosphoregulation of Lgl: Finding meaning  
559 in multiple on/off buttons. *Bioarchitecture* 6, 29–38.  
560 <https://doi.org/10.1080/19490992.2016.1149290>.
- 561 11. Holly, R.W., Jones, K., and Prehoda, K.E. (2020). A Conserved PDZ-Binding Motif in aPKC Interacts  
562 with Par-3 and Mediates Cortical Polarity. *Curr. Biol.* *CB* 30, 893–898.e5.  
563 <https://doi.org/10.1016/j.cub.2019.12.055>.
- 564 12. Atwood, S.X., Chabu, C., Penkert, R.R., Doe, C.Q., and Prehoda, K.E. (2007). Cdc42 acts  
565 downstream of Bazooka to regulate neuroblast polarity through Par-6 aPKC. *J. Cell Sci.* 120, 3200–  
566 3206. <https://doi.org/10.1242/jcs.014902>.
- 567 13. Hutterer, A., Betschinger, J., Petronczki, M., and Knoblich, J.A. (2004). Sequential Roles of Cdc42,  
568 Par-6, aPKC, and Lgl in the Establishment of Epithelial Polarity during *Drosophila* Embryogenesis. 6,  
569 845–854. <https://doi.org/10.1016/j.devcel.2004.05.003>.
- 570 14. Lee, C.-Y., Robinson, K.J., and Doe, C.Q. (2006). Lgl, Pins and aPKC regulate neuroblast self-  
571 renewal versus differentiation. *Nature* 439, 594–598. <https://doi.org/10.1038/nature04299>.
- 572 15. Bailey, M.J., and Prehoda, K.E. (2015). Establishment of Par-Polarized Cortical Domains via  
573 Phosphoregulated Membrane Motifs. *Dev. Cell* 35, 199–210.  
574 <https://doi.org/10.1016/j.devcel.2015.09.016>.
- 575 16. Dong, W., Zhang, X., Liu, W., Chen, Y.-J., Huang, J., Austin, E., Celotto, A.M., Jiang, W.Z.,  
576 Palladino, M.J., Jiang, Y., et al. (2015). A conserved polybasic domain mediates plasma membrane  
577 targeting of Lgl and its regulation by hypoxia. *J. Cell Biol.* 211, 273–286.  
578 <https://doi.org/10.1083/jcb.201503067>.
- 579 17. Betschinger, J., Mechtler, K., and Knoblich, J.A. (2003). The Par complex directs asymmetric cell  
580 division by phosphorylating the cytoskeletal protein Lgl. 422, 326–330.  
581 <https://doi.org/10.1038/nature01486>.
- 582 18. Peng, C.Y., Manning, L., Albertson, R., and Doe, C.Q. (2000). The tumour-suppressor genes lgl and  
583 dlg regulate basal protein targeting in *Drosophila* neuroblasts. *Nature* 408, 596–600.  
584 <https://doi.org/10.1038/35046094>.

- 585 19. Ohshiro, T., Yagami, T., Zhang, C., and Matsuzaki, F. (2000). Role of cortical tumour-suppressor  
586 proteins in asymmetric division of *Drosophila* neuroblast. *Nature* 408, 593–596.  
587 <https://doi.org/10.1038/35046087>.
- 588 20. Wirtz-Peitz, F., Nishimura, T., and Knoblich, J.A. (2008). Linking cell cycle to asymmetric division:  
589 Aurora-A phosphorylates the Par complex to regulate Numb localization. *Cell* 135, 161–173.  
590 <https://doi.org/10.1016/j.cell.2008.07.049>.
- 591 21. LaFoya, B., and Prehoda, K.E. (2021). Actin-dependent membrane polarization reveals the  
592 mechanical nature of the neuroblast polarity cycle. *Cell Rep.* 35, 109146.  
593 <https://doi.org/10.1016/j.celrep.2021.109146>.
- 594 22. LaFoya, B., and Prehoda, K.E. (2023). Consumption of a polarized membrane reservoir drives  
595 asymmetric membrane expansion during the unequal divisions of neural stem cells. *Dev. Cell*,  
596 S1534–5807(23)00159–4. <https://doi.org/10.1016/j.devcel.2023.04.006>.
- 597 23. Penkert, R.R., LaFoya, B., Moholt-Siebert, L., Vargas, E., Welch, S.E., and Prehoda, K.E. (2024). The  
598 *Drosophila* neuroblast polarity cycle at a glance. *J. Cell Sci.* 137, jcs261789.  
599 <https://doi.org/10.1242/jcs.261789>.
- 600 24. Moreira, S., Osswald, M., Ventura, G., Gonçalves, M., Sunkel, C.E., and Morais-de-Sá, E. (2019).  
601 PP1-Mediated Dephosphorylation of Lgl Controls Apical-basal Polarity. *Cell Rep.* 26, 293–301.e7.  
602 <https://doi.org/10.1016/j.celrep.2018.12.060>.
- 603 25. Lee, C.-Y., Andersen, R.O., Cabernard, C., Manning, L., Tran, K.D., Lanskey, M.J., Bashirullah, A.,  
604 and Doe, C.Q. (2006). *Drosophila* Aurora-A kinase inhibits neuroblast self-renewal by regulating  
605 aPKC/Numb cortical polarity and spindle orientation. *Genes Dev.* 20, 3464–3474.  
606 <https://doi.org/10.1101/gad.1489406>.
- 607 26. Oon, C.H., and Prehoda, K.E. (2019). Asymmetric recruitment and actin-dependent cortical flows  
608 drive the neuroblast polarity cycle. *eLife* 8. <https://doi.org/10.7554/eLife.45815>.
- 609 27. Oon, C.H., and Prehoda, K.E. (2021). Phases of cortical actomyosin dynamics coupled to the  
610 neuroblast polarity cycle. *eLife* 10, e66574. <https://doi.org/10.7554/eLife.66574>.
- 611 28. Hirata, J., Nakagoshi, H., Nabeshima, Y., and Matsuzaki, F. (1995). Asymmetric segregation of the  
612 homeodomain protein Prospero during *Drosophila* development. *Nature* 377, 627–630.  
613 <https://doi.org/10.1038/377627a0>.
- 614 29. Knoblich, J.A., Jan, L.Y., and Jan, Y.N. (1995). Asymmetric segregation of Numb and Prospero  
615 during cell division. *Nature* 377, 624–627. <https://doi.org/10.1038/377624a0>.
- 616 30. Spana, E.P., and Doe, C.Q. (1995). The prospero transcription factor is asymmetrically localized to  
617 the cell cortex during neuroblast mitosis in *Drosophila*. *Dev. Camb. Engl.* 121, 3187–3195.
- 618 31. Knoblich, J.A. (2010). Asymmetric cell division: recent developments and their implications for  
619 tumour biology. *Nat. Rev. Mol. Cell Biol.* 11, 849–860. <https://doi.org/10.1038/nrm3010>.
- 620 32. LaFoya, B., Penkert, R.R., and Prehoda, K.E. (2024). The cytokinetic midbody mediates asymmetric  
621 fate specification at mitotic exit during neural stem cell division. *BioRxiv Prepr. Serv. Biol.*,  
622 2024.08.27.609974. <https://doi.org/10.1101/2024.08.27.609974>.

- 623 33. Albertson, R. (2004). Scribble protein domain mapping reveals a multistep localization mechanism  
624 and domains necessary for establishing cortical polarity. *J. Cell Sci.* 117, 6061–6070.  
625 <https://doi.org/10.1242/jcs.01525>.
- 626 34. Besson, C., Bernard, F., Corson, F., Rouault, H., Reynaud, E., Keder, A., Mazouni, K., and  
627 Schweisguth, F. (2015). Planar Cell Polarity Breaks the Symmetry of PAR Protein Distribution prior to  
628 Mitosis in *Drosophila* Sensory Organ Precursor Cells. *Curr. Biol.* CB 25, 1104–1110.  
629 <https://doi.org/10.1016/j.cub.2015.02.073>.
- 630 35. Azuma, T., and Kei, T. (2015). Super-resolution spinning-disk confocal microscopy using optical  
631 photon reassignment. *Opt. Express* 23, 15003–15011. <https://doi.org/10.1364/OE.23.015003>.
- 632 36. Ho, J., Tumkaya, T., Aryal, S., Choi, H., and Claridge-Chang, A. (2019). Moving beyond P values:  
633 data analysis with estimation graphics. *Nat. Methods* 16, 565–566. [https://doi.org/10.1038/s41592-](https://doi.org/10.1038/s41592-019-0470-3)  
634 [019-0470-3](https://doi.org/10.1038/s41592-019-0470-3).
- 635

Figure 1

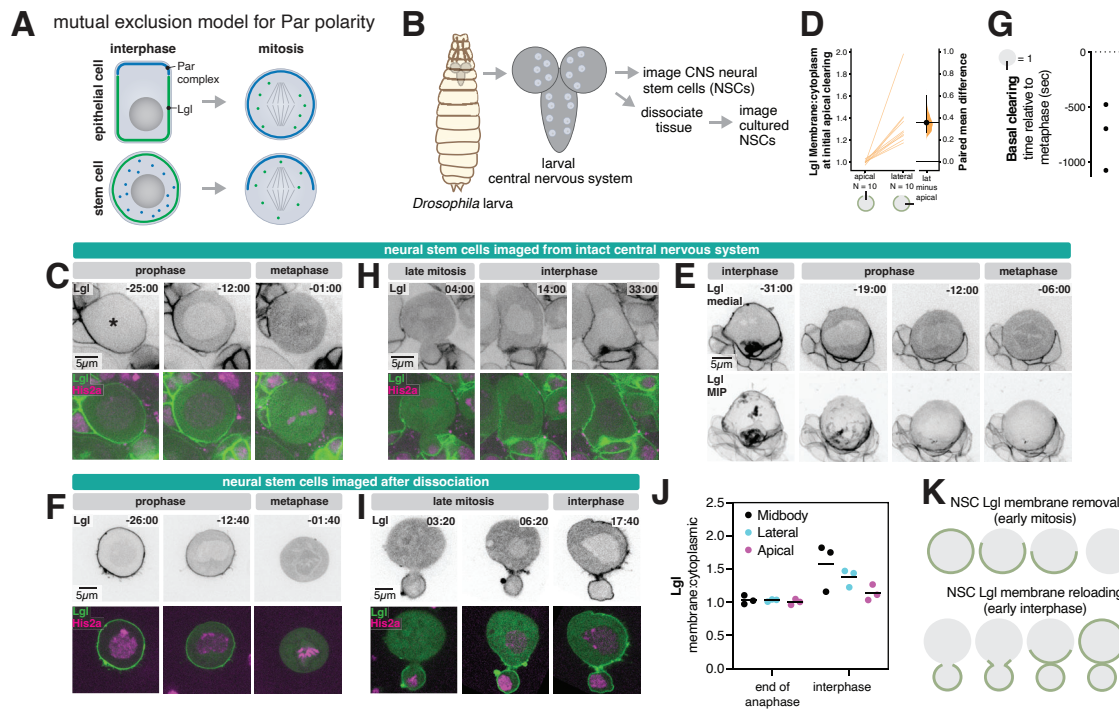


Figure 2

LaFoya et al.

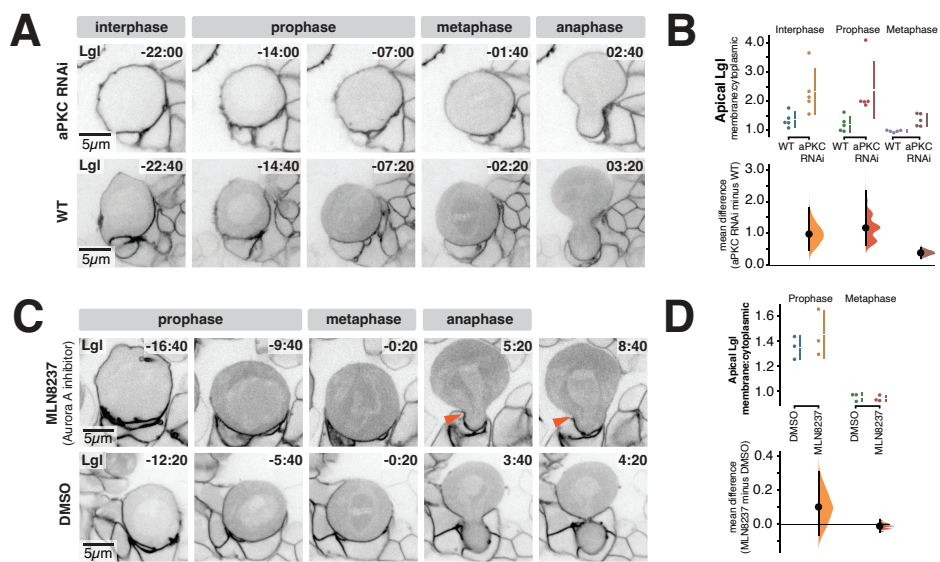


Figure 3

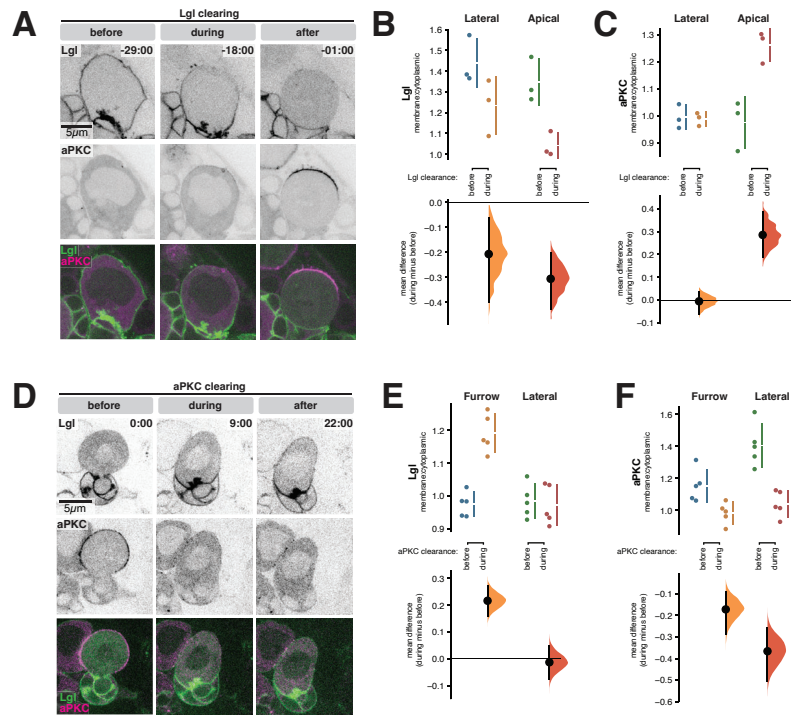


Figure 4

